Monitoring Gypsum Plaster Setting in a Foam through Raman Spectroscopy

Joachim Trosseille⬤, Gérard Panczer⬤, Christine Martinet⬤, and Marie Le Merrer⬤*

Université de Lyon, Université Claude Bernard Lyon 1, CNRS, Institut Lumière Matière, Villeurbanne F-69622, France

We use Raman spectroscopy to probe *in situ* the hydration reaction of a foamed mineral binder, here gypsum plaster. We show the strong effect of the mixing process used for foaming on the hydration kinetics. On the contrary, we observe no effect of the cationic surfactant tetradecyltrimethylammonium bromide (TTAB) used as foaming agent and of the foam structure. By tuning the hydration time scale with a setting retardant (citric acid) and measuring in parallel the characteristic bubble radius in the foam, we show that hydration kinetics control the arrest of the bubble-size evolution in the fresh foam and the final pore size in the set gypsum.

I. INTRODUCTION

Aerated mineral materials such as foamed concrete [1], foamed plaster [2], foamed calcium phosphate [3], or foamed geopolymers [4,5] are interesting because they combine the properties of the solid base material and those of air. They are therefore used for their lightness, as in gypsum plasterboards, their raw material content, which reduces the environmental footprint of Portland-cement production in foamed concrete, or their good thermal and phonic insulating properties [6]. They also have a large surface-to-volume ratio and hence a larger reactivity, which is interesting for their use in water treatment [5] or bone replacement [3,7].

A simple method to prepare such porous-mineral materials is to incorporate air mechanically into a hydraulic binder, i.e., a suspension of reactive particles that forms a solid through a dissolution-precipitation process [8,9]. The air can be incorporated either directly by strong shearing of the cementlike suspension or by mixing the reactive paste with a precursor foam [1,2,10].

Control of the macroscopic properties (the acoustic absorption, flow permeability, thermal conductivity, etc.) ideally requires tuning of the pore morphology, including the pore size [11,12]. It is determined both by the size of the air bubbles initially present in the fresh suspension foam and its evolution as the mineral binder sets. The fresh foam is indeed an unstable fluid structure, which evolves through the combined effects of gravity-induced drainage, ripening due to gas transfer between bubbles and bubble fusion called coalescence [13]. More precisely, for a given setting time, Feneuil *et al.* have shown that the stability of a cement foam is governed by the ratio between the

yield stress of the fresh material and the Laplace pressure, given by γ/R, where γ is the surface tension of the solution and R is the bubble radius [14]. However, so far, we do not know how this criterion evolves as the setting time is changed among various materials. More generally, the kinetics of dissolution-precipitation in mineral foams and its impact on the final porous structure have scarcely been explored [15].

The monitoring of setting reactions in mineral binders is often performed through calorimetry or x-ray diffraction [16–18] but it is not obvious to adapt these methods to *in situ* measurements inside a foam: the low thermal conductivity of foam must indeed disturb sample cooling in calorimetry, while x-ray diffraction usually probes samples on length scales much smaller than the bubble radius (typically 0.1–1 mm) and is thus not representative of the bulk of the foamed material.

The aim of the present study is therefore to show how *in situ* continuous Raman spectroscopy can be used to probe the kinetics of dissolution and precipitation of a foamed mineral binder, here gypsum plaster. We first investigate the influence of the surfactant and of the mixing process (mixing duration and velocity) used to generate the foam. We then study the role of the foam structure. Finally, the action of citric acid used as a setting retardant is studied. This allows us to modify the reaction kinetics and therefore the final pore size.

II. MATERIALS AND METHODS

A. Materials

1. Gypsum plaster

We study gypsum plaster as a model mineral binder. This material solidifies through a dissolution-precipitation

---

*marie.le-merrer@univ-lyon1.fr

034078-1

mechanism [16]. Plaster is the common name for calcium sulfate hemihydrate $CaSO_4 \cdot \frac{1}{2}H_2O$, also called bassanite when found in nature. It dissolves in water until solubility is reached (8.7 g/l at 25 °C, corresponding to 60 mM) [19]. Under these conditions, the ionic solution is supersaturated with respect to calcium sulfate dihydrate $CaSO_4 \cdot 2H_2O$, i.e., gypsum (solubility of 2.6 g/l, corresponding to 15 mM). This triggers the precipitation of gypsum needle-shaped crystals. The overall hydration can therefore be described by a single reaction:

$$CaSO_4 \cdot \frac{1}{2}H_2O + \frac{3}{2}H_2O \rightarrow CaSO_4 \cdot 2H_2O. \quad (1)$$
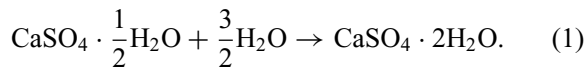
Finally, the entanglement of the gypsum needles provides the mechanical strength of the new mineral [20].

The plaster used is β-hemihydrate (plaster of Paris) from Fisher chemicals. The plaster-particle diameter distribution is measured by laser granulometry (Horiba LA-960) shortly after opening the jar. It is characterized by a median diameter Dv50 = 9.5 μm (for a volume-weighted distribution) and the first and last deciles Dv10 = 4.9 μm and Dv90 = 20.8 μm.

To make the plaster paste that is further foamed, the powder is dispersed in an aqueous solution containing surfactant and citric acid as a setting retardant. Control experiments without these organic additives are also performed for comparison.

Due to exposition to ambient air, the hygroscopic plaster evolves due to moderate hydration on the time scale of weeks. For each figure and parameter, the corresponding experiments are thus all performed within a limited period (1–2 weeks) and on a single batch.

2. Surfactant

The foaming agent used is the surfactant tetradecyltrimethylammonium bromide (TTAB, from Sigma-Aldrich). Unless specified, it is dissolved at concentration 3 g/l in deionized water. This corresponds to twice the critical micellar concentration (CMC) of TTAB in pure water. In solutions saturated with respect to gypsum, we measure that the CMC is lowered by a factor close to 2 (data not shown), due to the reduced electrostatic repulsion between the surfactant charged heads in the presence of sulfate ions [21]. In all cases, the surfactant concentration we use is thus well above the CMC.

According to zeta potential measurements from the literature, gypsum is positively charged ($\zeta \approx 20$ mV [22]) and plaster slightly positively charged ($\zeta \approx 4$ mV [23]). We therefore chose a cationic surfactant for which we expect a reduced adsorption compared to an anionic one, as supported by measurements of gypsum nucleation and growth for various surfactant charges [24].

3. Citric acid

We use citric acid (Acros Organics, purity >99%) to delay the setting time of the plaster. It is used at five different concentrations c_{CA} between 0 and 0.5 g/l. The main effect of citric acid is to hinder the growth of gypsum, by binding onto gypsum crystal faces [25]. Citric acid binding depends on the crystalline faces, which results in the same time in a change of the morphology of the crystals, from needlelike to more compact crystals [26–29]. As this changes the arrangement of the gypsum crystals in the final material, it is expected that the mechanical properties are also affected but both an increase [27] and a decrease [28] of mechanical strength with citric acid addition have been reported.

B. Methods

1. Sample preparation

The preparation protocol is summarized in Fig. 1(a). We first prepare a wet plaster by mixing the plaster powder and the solution with surfactant and citric acid. A fresh solution is prepared for each experiment. Throughout our whole study, the solution:plaster mass ratio (W/P) is kept equal to 0.8 unless specified. With 2750 kg/m^3 as the plaster density [30], this corresponds to a solid volume fraction of 0.31 in the initial suspension. The initial time $t = 0$ in our experiment is defined as the time when the plaster powder and the solution are put in contact. The wet plaster is mixed right afterward with an electric home blender equipped with a whisk (Bosch ErgoMixx) at a mixing rate ω_m during a mixing time t_m. The mixing rate ω_m depends on the choice of the blender mode (among three) and varies from 7 Hz to 17 Hz. The mixing time t_m is varied from 30 s to 120 s. To ensure a uniform and reproducible mixing, we use a foaming container of size comparable to the whisk (disposable 200-ml beaker) and we always make the same mass of plaster suspension (36.5 g).

Once the solution is foamed, it is transferred into one or two polystyrene Petri dishes of diameter 35 mm and height 10 mm, for further measurements detailed in the following paragraphs. It is closed to avoid evaporation from the peripheral bubbles. For the Raman spectroscopy measurements (see Sec. II B 4), the sample is sealed with a paraffin thin film to avoid the Raman signal from the polystyrene of the original cap.

In order to study the influence of the surfactant in two samples with the same structure (unfoamed) and under the same mixing procedure, we use the slightly different procedure presented in Fig. 1(b). (i) We prepare a sample of plaster and deionized water at mass ratio W/P = 0.8. (ii) The suspension is mixed at fixed conditions ($t_m = 60$ s, $\omega_m = 7$ Hz). (iii) It is gently mixed with a spatula with a surfactant solution at concentration 15 g/l, to obtain a final sample at mass ratio W/P = 1 and a surfactant concentration of 3 g/l in the solution. This allows us to prepare a
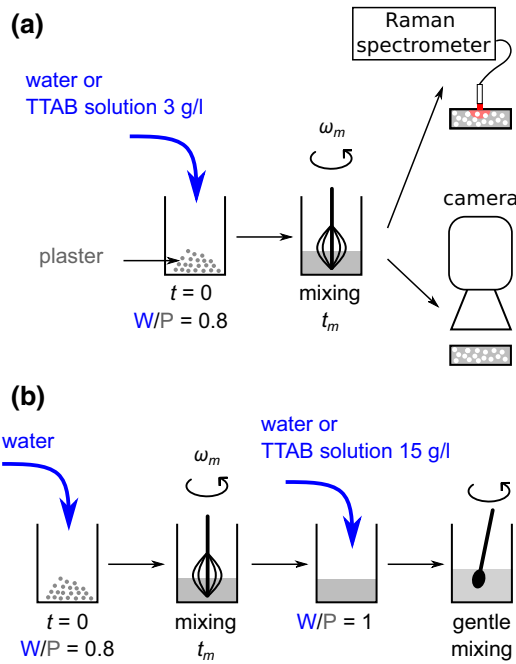
FIG. 1.   (a) The preparation protocol used in most of our experiments. (b) The special protocol to study the influence of the surfactant (see text for details).

FIG. 2.   The air-volume fraction ϕ incorporated in the foamed plaster suspension, as a function of the mixing time t_m for different mixing rates ω_m. The dashed lines show the extrapolation to $\phi = 0$ when the suspension is not mixed ($t_m = 0$ s). The TTAB surfactant solution is used at concentration 3 g/l, except for the hollow square (no surfactant). The error bars for $\omega_m = 17$ Hz illustrate the reproducibility of the measurement.

mixed unfoamed sample but still one that contains surfactant. The same procedure is used for the sample without surfactant, replacing the incorporated surfactant solution in step (iii) by deionized water.

2. Air-volume fraction

The air-volume fraction ϕ entrained in the foamed plaster is deduced from sample weighing through the relation $\phi = 1 - m/(\rho_s V)$, where m and $V = 9.6$ ml are the mass and volume of plaster foam inside the Petri dish and $\rho_s = 1550$ kg/m^3 is the density of the initial plaster suspension. It is only slightly smaller than the density of the final water-plus-gypsum material (1600 kg/m^3), considering the plaster and gypsum densities (2750 and 2320 kg/m^3 [30]) and the reaction stoichiometry, so we neglect the corresponding volume variation.

We first evaluate the volume fraction of air entrained by the mixing process in the plaster suspension when no foaming agent is present. We find that it is rather limited ($\phi = 3.6 \pm 0.6\%$ for $t_m = 60$ s and $\omega_m = 17$ Hz).

For plaster mixed with the surfactant solution (TTAB at 3 g/l), Fig. 2 shows the final air-volume fraction ϕ as a function of the mixing time t_m, for different rotation speeds ω_m. We observe that the air volume entrained is more than one order of magnitude larger than without surfactant (ϕ in the range 55%–93%). We also find that the air-volume fraction increases with the rotation speed. Depending on
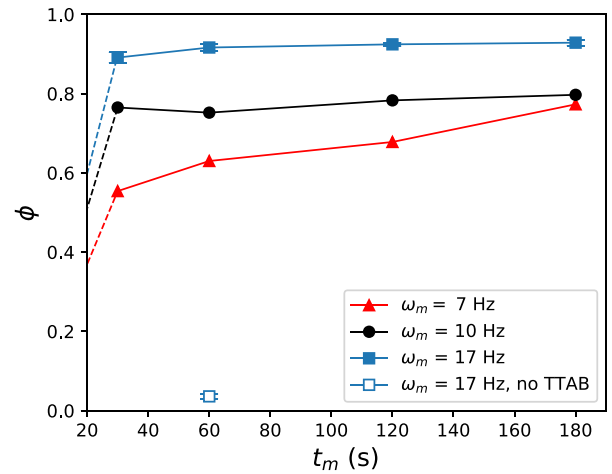
ω_m, ϕ either increases ($\omega_m = 7$ and 10 Hz) or remains constant with t_m ($\omega_m = 17$ Hz).

This result is consistent with the findings of Politova et al. [31] for aqueous foams (without particles) under shear mixing in a similar kitchen mixer. They have observed that the volume of air entrained increases with time and then saturates and that the final air fraction is larger and reached sooner when increasing the mixing rate ω_m. The authors explain the evolution of the foam volume by the following mechanism. In the first stage (gas fraction increasing with time), air is entrapped following breaking of waves at the foam surface. This process is more efficient at high shear rates or velocities, as observed in other self-aerating devices such as plunging jets or breaking waves [32]. In the meantime, the trapped bubbles are broken apart under shear so that the average bubble size decreases. Both mechanisms increase the shear stress in the foam. This damps the surface waves, leading to the arrest of air entrainment and the saturation of ϕ that we observe for $\omega_m = 10$ and 17 Hz.

3. Bubble-size measurements

For experiments on the effect of setting retardant (citric acid), we image the top surface of the plaster-foam sample with a CCD camera (IDS uEye) equipped with a lens. The lens magnification is chosen as a compromise to measure both the bubble size at the initial stage (smaller bubbles) and the final one (fewer bubbles). An image of the surface is recorded every 4 s. An example of the evolution of the foam structure is shown in Fig. 3 (see also the video in the Supplemental Material [33]).
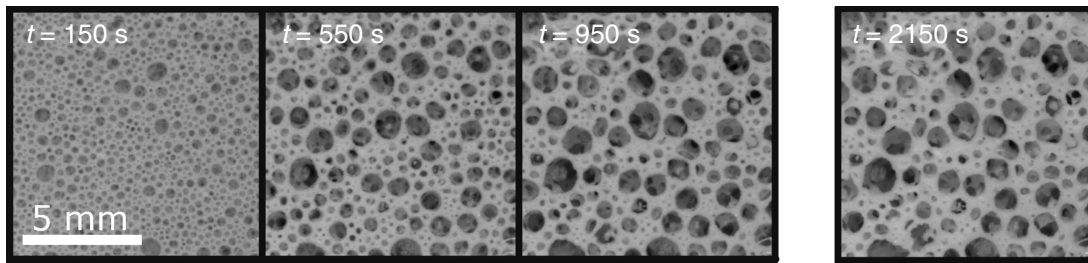
FIG. 3. The evolution of the foam top surface with time t. Experimental conditions: $t_m = 60$ s, $\omega_m = 17$ Hz, surfactant concentration 3 g/l, citric acid concentration $c_{CA} = 0.5$ g/l.

We first observe on such images the average growth of the bubbles, termed coarsening or ripening: due to differences in Laplace pressures, the gas contained in the smaller bubbles dissolves in the liquid and diffuses to the larger ones through the liquid films. The larger bubbles therefore grow, the smaller ones eventually disappear, and the average bubble size increases [13].

We also observe that the surfactant efficiently prevents soap-film rupture, as no coalescence (bubble-merging) events are observed. In addition, no plaster particles are present in the soap films. After setting, we therefore obtain an open-cell porous material (connected pores).

To evaluate the importance of drainage, we compare images of the top and bottom surfaces after setting for the longer setting kinetics (citric acid at the largest concentration 0.5 g/l). The apparent surface-gas volume fraction is 0.47 ± 0.01 at the bottom, versus 0.52 ± 0.01 at the top ($t_m = 60$ s, $\omega_m = 17$ Hz), corresponding to a relative variation of 10%. We therefore neglect it and consider that the evolution of the bubble structure is mainly due to coarsening.

Image analysis using the FIJI software package [34] and the procedure detailed in Appendix A allows us to measure the radii R_i of typically 400–1500 surface bubbles and to determine the Sauter radius of the bubble-size distribution, defined as $R_{32} = \sum R_i^3 / \sum R_i^2$. R_{32} is found to vary between 150 and 450 μm depending on time and experimental conditions. Although the bubble-size distribution at the surface may not be fully representative of that in bulk [35,36], it has been shown previously that bubbles at the boundary and in bulk coarsen in pace [37]. We therefore consider the surface Sauter radius R_{32} to be representative of the bulk foam structure, which can then be monitored without sample destruction.

4. Monitoring of the hydration reaction with Raman spectroscopy

We use Raman spectroscopy to follow the hydration reaction. As the plaster sets, calcium sulfate hemihydrate dissolves and dihydrate (gypsum) precipitates. This change of crystalline environment is associated with frequency changes in the vibration modes of sulfate molecules, which are monitored through Raman spectroscopy.

We use an Ocean Insight Raman spectrometer (QE65000) working at $\lambda = 785$ nm with a resolution of 2 cm^{-1}. It is equipped with a backscattering probe that brings the laser light to the top surface of the mineral-foam sample and sends the backscattered light to the spectrometer. The laser power is set to 170 mW and the acquisition duration is varied between 4 and 30 s. This is much smaller than the time scale of hydration, so we can smooth the time-resolved data in the figures for clarity.

Unless specified, the sample is placed on a turntable working at approximately 4 revolutions per minute. Otherwise, we find unreproducible results for the foamed samples and long setting times, which we attribute to local heating due to prolonged laser exposition and reduced heat transport in the foamed material (compared to bulk). The Raman signal is therefore averaged from various locations at the top of the sample. Finally, to obtain absolute measurements of the Raman shift, the Raman spectrometer is calibrated with a reference synthetic quartz with a known and well-defined peak at 465 cm^{-1}.

The size of the region probed by the Raman setup is determined by the width of the laser beam at the sample surface, typically of the order of 1 mm, and the depth of penetration of the laser light inside the foamed suspension, a medium that scatters light. The depth of the scattering volume is estimated as a few times ℓ^*, the light-transport mean free path [38]. On the one hand, the light-transport mean free path of light in a liquid foam is proportional to the bubble radius: $\ell^* \approx 4 - 6R$ for the gas fractions studied in our work [39]. This corresponds to $\ell^* \approx 0.6$–3 mm. On the other hand, the light-transport properties of the reacting plaster suspension are not known and are expected to evolve upon time. A rough estimate is, however, provided by Mie scattering solution. Taking into account the median plaster-particle diameter of approximately 10 μm, we find ℓ^* of the order of 100 μm for the (unfoamed) plaster slurry. This is comparable to the initial bubble radius (typically 150 μm; see Sec. III B). Some scattered light must thus reach the second layer of bubbles from the surface. Finally, the determination of the precise value of the penetration depth is beyond the scope of this study

but we expect it to be intermediate between the two esti-mated above, of the order of 1 mm and larger than a bubble diameter. We therefore consider the Raman mea-surements as reasonably representative of the bulk of the foam.

For a quantitative analysis of the Raman signal, we focus on the most prominent ν_1 peak, corresponding to the symmetric stretching vibration mode of SO_4 groups [40]. Figure 4 shows an example of the evolution of the Raman signal (the scattered intensity as a function of the Raman-shift wave number ν) in the range $\nu = 960$–1060 cm^{-1}, as hydration proceeds during the setting of a foamed gypsum-plaster sample. The signals from hemihydrate (plaster powder) and dihydrate (gypsum powder from
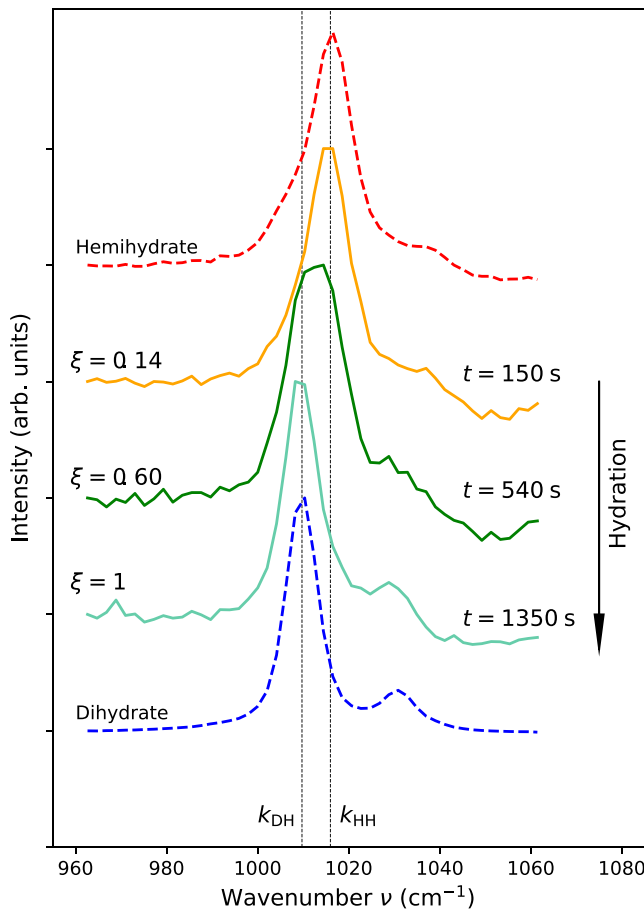
Acros Organics), measured separately, are also shown for comparison (dashed lines). The locations of the ν_1 peaks of pure hemihydrate and dihydrate are, respectively, $k_{HH} = 1016.0$ cm^{-1} and $k_{DH} = 1009.7$ cm^{-1} and are consistent with values reported in the literature [41]. We observe that during the setting, the characteristic wave number k of the peak decreases with time from $k_i = 1015.1$ cm^{-1} at $t = 150$ s to $k_f = 1009.7$ cm^{-1} at $t = 1350$ s. This is indicative of the advancement of the hydration reaction of calcium sulfate. Note that the initial peak location k_i is slightly different from the pure hemihydrate peak k_{HH}. This shows that hydration starts before the first Raman spectrum, during the first 150 s of the experiment, corre-sponding to the mixing and setup of the sample. On the other hand, $k_f \approx k_{DH}$, indicating that hydration is almost complete at the end of the experiment.

Finally, to extract the location $k(t)$ of the ν_1 peak with a finer resolution, we fit each spectrum using a Lorentzian function and we calculate the extent of the setting reaction as

$$\xi(t) = 1 - \frac{k(t) - k_f}{\Delta k_{th}}, \qquad (2)$$

where $\Delta k_{th} = k_{HH} - k_{DH} = 6.3$ cm^{-1}. More details on the fitting procedure and its interpretation can be found in Appendix B. Examples of the reaction kinetics $\xi(t)$ are shown in Fig. 5, from which a characteristic reaction time τ_{chem} can be defined as $\xi(t = \tau_{chem}) = 1/2$.

FIG. 4. Raman spectra showing the transition of peak $\nu_1(SO_4)$ during the hydration reaction in a foamed sample ($t_m = 60$ s, $\omega_m = 17$ Hz, TTAB 3 g/l, no citric acid): the intensity (offset for clarity) is shown as a function of the Raman-shift wave num-ber ν. The plain lines correspond to the Raman peak of the foamed plaster at $t = 150$, 540, and 1350 s, corresponding to extent of reaction $\xi = 0.14$, 0.60, and 1, respectively. The dashed lines correspond to hemihydrate (plaster) and dihydrate (gyp-sum) Raman bands as measured separately on reference powders. k_{HH} and k_{DH} are the corresponding peak positions.
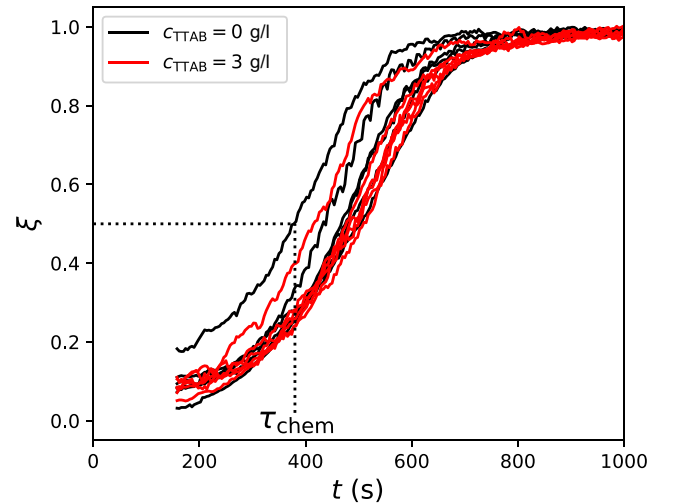

FIG. 5. The extent of the reaction ξ as a function of time t with TTAB surfactant (light red) and without surfactant (black). Each experiment is repeated 6 times. Final W/P = 1. Experimental conditions: $t_m = 60$ s, $\omega_m = 7$ Hz, no citric acid.

III. RESULTS

A. Kinetics of hydration in a gypsum-plaster foam

1. Surfactant

We aim at comparing plaster setting kinetics in bulk and in foam conditions. Two things are necessary to make a foam: a foaming agent (surfactant) and the foaming process, which here is induced by mixing. In this paragraph, we first evaluate the role of the surfactant alone on the hydration kinetics. In order to keep the same mixing conditions in two samples with the same structure (unfoamed), we thus use the modified preparation protocol presented in Fig. 1(b) and in Sec. II B 1.

Figure 5 compares the hydration kinetics measured with and without surfactant. It shows that the TTAB surfactant at concentration 3 g/l is neutral in the reaction process. This is consistent with the expectation of limited interactions between the positively charged surfactant and calcium sulfate minerals (see Sec. II A).

2. Foaming process

We focus in this study on mineral foams obtained by strong mixing. This procedure is commonly used to generate particle-laden foams due to its simplicity [2,42,43] and we wonder here about the extent to which it affects the setting kinetics.

We therefore investigate the influence of the mixing time t_m and mixing rate ω_m on the setting kinetics of a plaster suspension without a foaming agent (surfactant). As no surfactant is present, the plaster remains unfoamed.

The mixing time is varied from 30 s to 120 s. Outside this range, the mixing time is either too short to provide sufficient homogenization of the solution or too long to avoid significant hydration. Two mixing rates are selected: $\omega_m = 7$ Hz and $\omega_m = 17$ Hz. Hand mixing is also investigated but leads to nonreproducible results. Two sets of experiments are performed at different citric acid (CA) concentrations.

Figure 6 shows the extent of reaction ξ as a function of time t for different mixing durations t_m and rates ω_m. The two subfigures correspond to different citric acid concentrations, $c_{CA} = 0$ [Fig. 6(a)] and $c_{CA} = 0.5$ g/l [Fig. 6(b)]. We observe that the plaster setting kinetics are accelerated by a factor close to 1.6 when the mixing time is increased by a factor of 4. The influence of the mixing rate is less obvious: increasing ω_m decreases the setting time for pure plaster but has no effect when citric acid is present.

To summarize, the strong shear applied on the plaster suspension during the foaming process, in the first minutes of the experiment, has a significant effect on the subsequent hydration kinetics (from a few to a few tens of minutes) and must be rigorously controlled to provide reproducible results. In the following, we therefore fix the mixing time
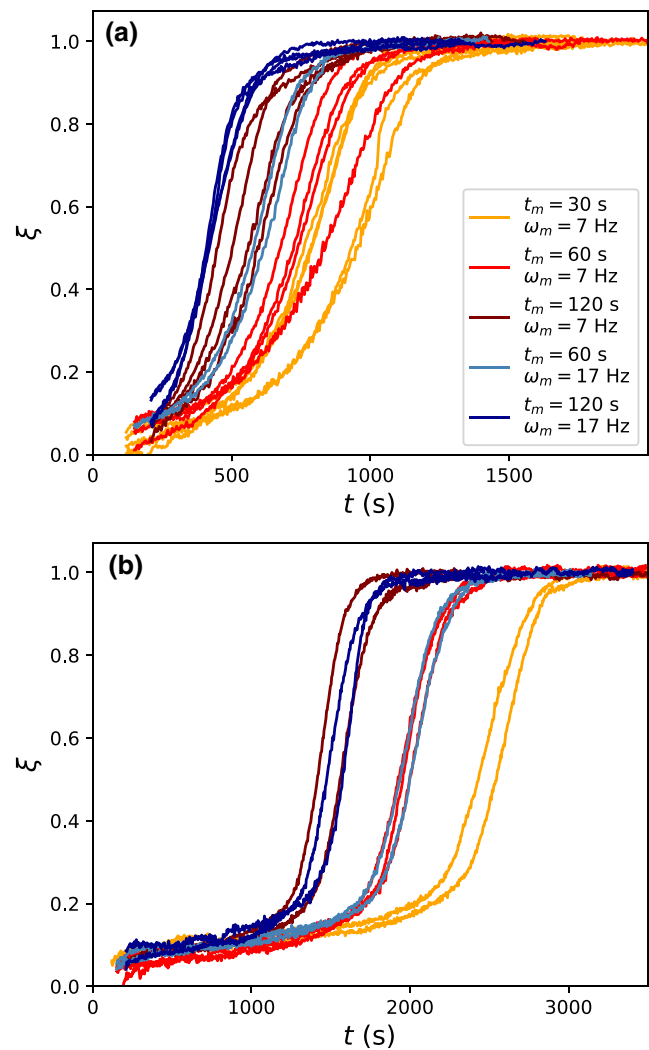

FIG. 6. The extent of the reaction ξ as a function of time t for different mixing times t_m, mixing rates ω_m, and citric acid concentrations (a) $c_{CA} = 0$ and (b) $c_{CA} = 0.5$ g/l. Several experiments are done in the same conditions to illustrate the reproducibility of the measurements. No surfactant is used, so the samples are unfoamed. The measurements are obtained at a fixed location in the sample (no turntable).

to $t_m = 60$ s and each set of curves is obtained for a constant mixing rate ω_m.

3. Comparing setting kinetics in a foamed and in a bulk material

We now know that plaster hydration kinetics hardly depend on the presence of TTAB surfactant but are strongly affected by the mixing process. By imposing the same mixing conditions on samples containing or not containing surfactant, we can now investigate the role of the foam geometry (obtained by mixing in the presence of surfactant), compared to setting in a bulk material (no surfactant). These results are shown in the $\xi(t)$ curves of
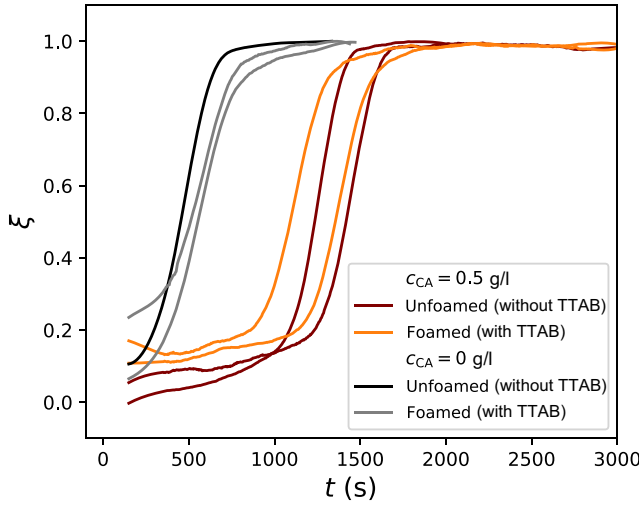
FIG. 7. The extent of the reaction ξ as a function of time t for $c_{CA} = 0$ and 0.5 g/l. Samples are either foamed (with surfactant TTAB at concentration 3 g/l) or unfoamed (without surfactant). Experimental conditions: $t_m = 60$ s, $\omega_m = 17$ Hz.

Fig. 7. We find no observable influence of the foam structure, compared to the bulk material, both with and without citric acid. In both cases, the difference in the characteristic setting time τ_{chem} is smaller than or comparable to the dispersion of similar measurements (typically 200–300 s with citric acid and 100 s without citric acid; see Fig. 6).

4. Citric acid

Figure 8(a) shows the influence of the citric acid concentration c_{CA} on the hydration kinetics in foamed plaster for other experimental conditions fixed (TTAB 3 g/l, $t_m = 60$ s, $\omega_m = 17$ Hz, W/P = 0.8). As expected (see II A), we observe that citric acid acts as a setting retardant, the hydration time τ_{chem} increasing by a factor close to 2 as c_{CA} increases from 0.1 to 0.5 g/l. We find no noticeable difference between $c_{CA} = 0$ and 0.1 g/l. Preliminary experiments also show that the retarding effect saturates above 0.5 g/l.

B. Evolution of foam structure

For citric acid concentrations in the range $c_{CA} = 0.1 - 0.5$ g/l, we measure the temporal evolution of the Sauter radius R_{32} in parallel to the Raman measurements of Sec. III A 4. Our results are shown in Fig. 8(b).

For each experiment, we initially observe an increase of the Sauter radius R_{32} due to coarsening, before a plateau R_{max} is reached as the interstitial suspension becomes a solid mineral. As the citric acid concentration increases and the setting reaction is delayed, we observe that the time τ_{mech} to reach the saturation logically increases. This results in a larger pore radius in the final material, though with some experimental variability.
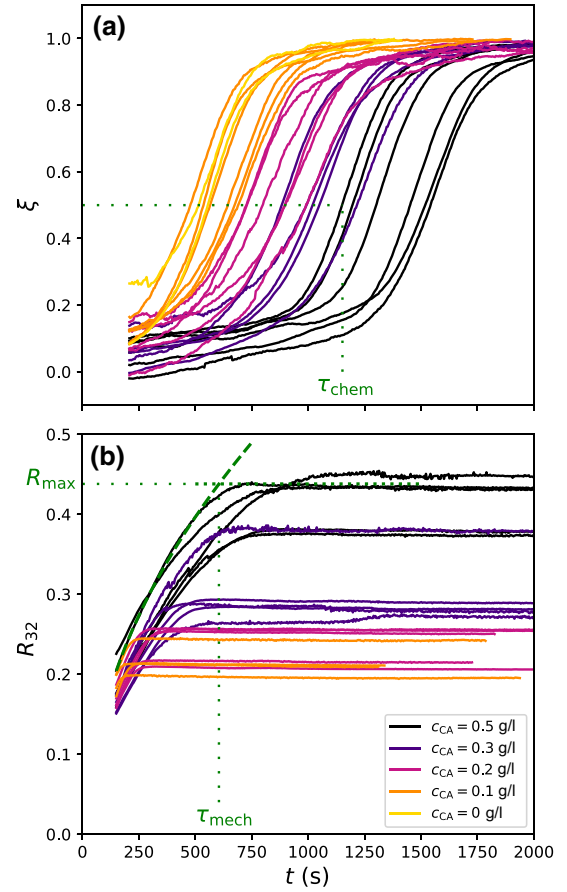

FIG. 8. (a) The extent of the reaction ξ as a function of time t for different citric acid concentrations c_{CA}. The dashed lines show the definition of τ_{chem} for one specific experiment. (b) The Sauter radius R_{32} as a function of time for different citric acid concentrations c_{CA}. For the same specific experiment as in (a), the dashed line corresponds to a fit by Eq. (3) for coarsening dynamics, with $D_c = 3.3 \times 10^{-4}$ mm^2/s (see Sec. IV B). The dotted line shows the maximum radius R_{max} obtained at the end of the experiment. τ_{mech} is defined as the intercept between the two curves and characterizes the arrest of coarsening of each experiment. Experimental conditions: $t_m = 60$ s, $\omega_m = 17$ Hz, TTAB concentration 3 g/l.

IV. DISCUSSION

A. Kinetics of hydration

We first discuss the shape of the reaction curves $\xi(t)$ and the corresponding time scales.

The kinetics of the hydration reaction can be limited by various mechanisms: (i) the dissolution of hemihydrate, (ii) the diffusion of reactants in the suspending liquid from a hemihydrate particle to a gypsum crystal, and (iii) the nucleation and growth of gypsum crystals.

We first estimate the maximum diffusive flux that can be achieved in our system. From the solubilities of gypsum and plaster, the maximum concentration difference of calcium sulfate in the liquid is $\Delta c = 60 - 15 = 45$ mM.

We consider rather dense suspensions (solid volume fraction of the order of 0.3) so the interparticle distance δ must be close to the particle size, typically 10 μm for the initial plaster powder. Taking the diffusion coefficient $D \approx 10^{-9}$ m^2/s, we obtain the diffusive flux $j_D \approx D\Delta c/\delta \approx 5$ mmol/m^2/s.

When undergoing mixing, the suspension becomes strongly sheared. Characterizations of flows of similar kitchen mixers [44] have shown that they can reach shear rates $\dot{\varepsilon}$ of typically 10–30 $\omega \approx 170$–500 s^{-1}. This results in diffusive boundary layers of thickness $\delta_{BL} \sim \sqrt{D/\dot{\varepsilon}} \approx 2$ μm. This is smaller than, yet comparable to, the interparticle distance, so the enhancement of reactant transport through advection must be limited.

On the other hand, the reactivity of the gypsum and plaster surfaces can be estimated from the dissolution rate of gypsum $k \approx 40$ μmol/m^2/s reported in the literature [45]. This is 2 orders of magnitude lower than the diffusive flux j_D, so we estimate that the precipitation of dihydrate and the dissolution of hemihydrate are the limiting mechanisms of the reaction.

More precisely, the reaction advancement follows three stages highlighted in the inset of Fig. 9 [19,46,47]. First, there is an induction period (I) during which the limiting steps are heterogeneous nucleation and the initial growth of gypsum crystals onto the plaster grains. Second, there is a rapid increase of the reaction (II), limited by the growth of the gypsum crystals. Third, the reaction starts to slow down (phase III in the inset of Fig. 9), limited by the dissolution of the remaining plaster particles. As a first approximation, we estimate the duration of these three phases as $\tau_I = t(\xi = 0.2)$, $\tau_{II} = t(\xi = 0.7) - t(\xi = 0.2)$, and $\tau_{III} = t(\xi = 0.9) - t(\xi = 0.7)$, respectively. We report in Fig. 9 the variations of these three time scales with the average duration τ_{chem}.

Figure 9(a) shows the effect of citric acid on the characteristic durations τ_I, τ_{II}, and τ_{III}. We observe that the increase of the hydration time scale τ_{chem} upon citric acid addition can be mostly attributed to the increase of the induction time τ_I and, to a lesser extent, to the increase of the duration of the growth-limited phase τ_{II}. The phase (III) limited by plaster dissolution is barely affected. This is consistent with the literature, highlighting the interaction of citric acid with the gypsum surfaces [25–29].

We now discuss the influence of the mixing procedure highlighted in Sec. III A 2, where we show that the time scale for hydration τ_{chem} is shorter after longer mixing (larger t_m) and, to a lesser extent, for faster rotation rates (larger ω_m). Note that the retarding effect on the reaction duration [typically 1000 s on Fig. 6(b)] can be much larger than the initial difference in mixing duration (90 s). Similar effects have previously been observed in Refs. [48,49].

Figure 9(b) shows the influence of the mixing duration on the three phases of the hydration reaction. In this case, we observe that the three characteristic time
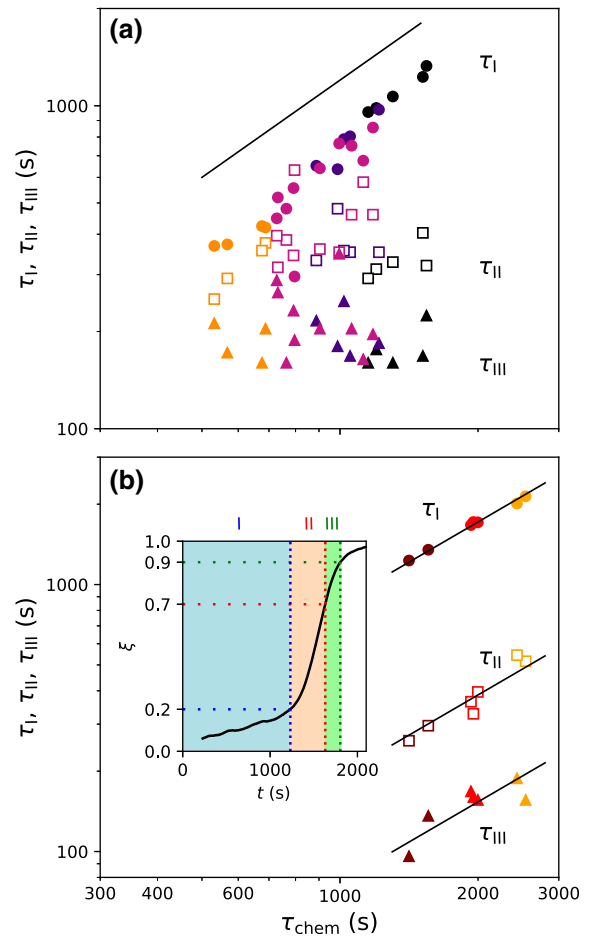

FIG. 9. The characteristic time scales of the three phases of hydration τ_I (induction), τ_{II} (growth-limited), and τ_{III} (dissolution-limited), as a function of the average duration τ_{chem}. (a) The influence of the citric acid concentration, increasing from left to right (same colors as in Fig. 8). The line corresponds to a linear behavior $\tau \sim \tau_{chem}$. (b) The influence of the mixing duration t_m, decreasing from left to right (same colors as in Fig. 6), $c_{CA} = 0.5$ g/l, $\omega_m = 7$ Hz. The lines show the linear fits of the data. The inset shows a typical hydration curve $\xi(t)$ highlighting the three phases of the reaction.

scales are proportional to the average duration τ_{chem}. This indicates that gypsum nucleation and growth and plaster dissolution are equally affected by the induced shear. As discussed above, we expect advection-diffusion to play a limited role in the reaction. However, it has been previously observed that shear induced by the mixing can hinder the aggregation of gypsum needles [48]. A similar effect can be expected for the plaster particles. This mechanism will increase the gypsum surface area available for precipitation and the plaster surface area prone to dissolution. Besides, previous experiments on suspensions of attractive particles have shown that larger shear rates lead to smaller aggregates [50,51], which could explain the (small) effect of the mixing rate ω_m on the
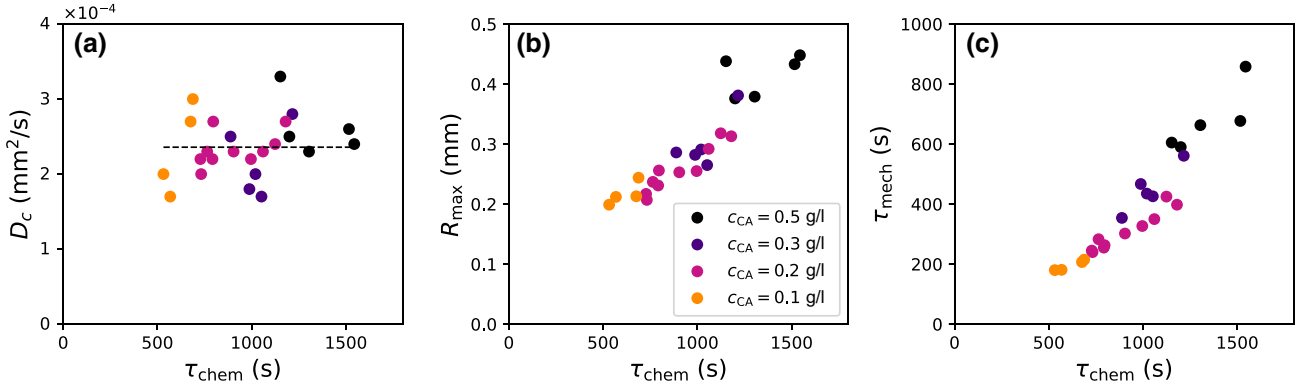
FIG. 10.　(a) The effective diffusion coefficient D_c for coarsening dynamics, (b) the maximum Sauter radius R_{max}, and (c) the mechanical time for coarsening arrest τ_{mech}, as a function of the hydration time τ_{chem} for various citric acid concentrations c_{CA} (colors). The horizontal line in (a) shows the average value $D_c = (2.4 \pm 0.4) \cdot 10^{-4}$ mm^2/s. Experimental conditions: $t_m = 60$ s, $\omega_m = 17$ Hz, foamed samples (surfactant TTAB at 3 g/l).

hydration kinetics [see Fig. 6(a) for samples without citric acid]. Further investigation is, however, necessary to demonstrate the role of particle disaggregation or disentanglement unambiguously. Finally, it should be recalled that the samples are unfoamed in this set of experiments, as no surfactant is present; therefore, the effects observed in Figs. 6 and 9(b) cannot be attributed to dynamical processes specific to foams, such as bubble rearrangements or bubble coalescence.

B. Controlling pore size through setting time

We now focus on the bubble-size evolution in the foam. As shown in Fig. 8(b), we observe that the bubble Sauter radius first increases due to coarsening, before reaching a plateau R_{max} corresponding to the solidification of the interstitial gypsum structure. As the concentration of setting retardant (citric acid) increases, the plateau is reached later, leading to a larger pore size in the final material. This is consistent with the findings of Roch Isern *et al.* [15], who have observed a smaller pore size in gypsum foams in the presence of setting accelerator (gypsum seeds).

More quantitatively, coarsening in three-dimensional aqueous foams is known to follow diffusive dynamics controlled by gas transport in the liquid films [52]:

$$R_{32} = \sqrt{R_1^2 + D_c(t - t_1)}, \qquad (3)$$

where R_1 the Sauter radius at time t_1 and D_c is an effective diffusion coefficient controlled mainly by the gas fraction ϕ and the foam physico-chemistry (gas and surfactant nature). We find that our $R_{32}(t)$ data at short times are well fitted by Eq. (3), as shown for one example in Fig. 8(b) (green dashed line). This allows us to determine D_c for each experiment. Finally, we also determine the final radius R_{max} and the characteristic time τ_{mech} for the arrest of coarsening, defined as the intersection

between the initial coarsening law and R_{max} [see Fig. 8(b)]. This mechanical time characterizes the solidification of the foam structure. We now discuss how these parameters depend on the hydration time scale τ_{chem}.

We first plot the effective diffusion coefficient D_c, characterizing the early coarsening process, as a function of the chemical time τ_{chem} obtained from Raman spectroscopy measurements, for various citric acid concentrations [Fig. 10(a)]. We observe that D_c is roughly constant when τ_{chem} and c_{CA} vary, with $D_c = (2.4 \pm 0.4) \cdot 10^{-4}$ mm^2/s. This value has the same order of magnitude as those reported for particle-free aqueous foams [52]. This indicates that the plaster hydration reaction plays no role in coarsening in the fresh foam.

Figure 10(b) shows the final Sauter radius R_{max} as a function of τ_{chem}. We observe that R_{max} increases with the hydration characteristic time. This shows that retardation or acceleration of setting can be used as a means to control the pore size of foamed minerals. For fixed experimental conditions (constant citric acid concentration), we find that the variability of the final radius is mostly due to the variability of the hydration kinetics.

Finally, the increase of the final radius with the hydration time τ_{chem} is a direct consequence of the increase of the mechanical time τ_{mech} at which coarsening is arrested. This behavior, shown in Fig. 10(c), is expected since the mechanical strength of the final material stems from the entanglement of the gypsum needles resulting from hydration. Similarly to the case of R_{max}, we observe that, for a fixed citric acid concentration, the apparent dispersion in mechanical time coincide with variations in hydration time. We also observe that τ_{mech} is smaller, by a factor of between 2 and 3, than the characteristic time for hydration τ_{chem}. This is also visible in Fig. 8, where the two subfigures share the same time axis and the two time scales τ_{chem} and τ_{mech} are determined for the same experiment. This fact indicates that the foam structure stops evolving

in the first stages of the hydration reaction. We find that it corresponds to $\xi(t = \tau_{\text{mech}}) \approx 0.1$. However, the two characteristic times are not strictly proportional: as τ_{chem} goes from 750 to 1500 s (factor 2), we find that τ_{mech} varies from 250 to 750 s (factor 3). This is because the time scales of the three phases of the reaction highlighted in Fig. 9 do not grow in pace when the citric acid concentration is varied.

Previous works have shown that the arrest of coarsening is controlled by the ratio between the Laplace pressure γ/R_{32}, which drives coarsening, and the resistance of the solid interstitial network, characterized either by its yield stress σ_Y [14] or its shear modulus G [53]. The first Laplace term decreases with time, at most by a factor of 3 [Fig. 8(b)], while G increases by orders of magnitude in the first minutes of setting [54]. The instant of coarsening arrest τ_{mech} must therefore be primarily controlled by the change of rheological properties of the paste. Our results highlight that this corresponds to the beginning of the hydration reaction ($\xi \approx 0.1$). Further investigations should focus on relating the hydration reaction kinetics to the evolution of the rheological properties of the reactive foamed paste in the early times of solidification. This relation can indeed be affected by several parameters: (i) the presence of additives (such as citric acid) can change the gypsum microstructure; (ii) foams that set later undergo structure rearrangements (bubble reorganizations) when coarsening, which could delay stiffening; and (iii) the confinement induced by the foam network has previously been found to modify the rheology of nonreactive suspensions [55,56].

V. CONCLUSIONS

In this study, we show that *in situ* continuous Raman spectroscopy can be used to probe the kinetics of hydration of a mineral in a foamed suspension.

The effect of foaming on the hydration of gypsum plaster is investigated. We show that the presence of TTAB cationic surfactant and the foam structure in itself have no detectable influence on the setting kinetics. However, the foaming process, which involves strong suspension shearing at the beginning of the reaction, significantly modifies the subsequent hydration kinetics, probably by disaggregating the growing gypsum and dissolving plaster crystals.

Finally, by using citric acid as a setting retardant, we are able to modify the pore size of the final material. This quantity is determined by the competition between the fresh foam aging due to coarsening and the stiffening of the foamed material following hydration. Increasing the hydration time scale with retardant therefore results in later coarsening arrest and larger bubble radius. We also find that coarsening arrest takes place at an early stage of plaster hydration.

From a practical point of view for the elaboration of mineral foams (foamed cement, concrete, geopolymer,

etc.), this implies that a good control of the hydration kinetics is crucial to tune the final pore size in the solid material.

As Raman spectroscopy is applicable in other kinds of hydraulic binders such as Portland cement [57,58], our technique could be adapted to probe the reaction kinetics of various types of aerated mineral materials and to relate the hydration degree to mechanical stiffening of the foam. In particular, an interesting situation would be to investigate closed-cell foams [59], where hydration also proceeds in the thin films separating the pores.

APPENDIX A: IMAGE PROCESSING FOR BUBBLE-RADIUS MEASUREMENT

A set of operations is performed on each image, as shown in Fig. 11, using the FIJI software package. The raw image [Fig. 11(a)] is first duplicated. A Gaussian blur filter with radius 25 px corresponding to approximately 700 μm is applied to the copy and subtracted from the raw image. This gives the image shown in Fig. 11(b), where only the top bubbles are visible. An intensity threshold (value 0) is applied to convert the image in Fig. 11(b) into a binary image [Fig. 11(c)]. "Fill Holes" and "Watershade" operations are then carried out on the binary image to ensure proper segmentation between neighboring bubbles. Figure 11(c) is the final image, on which bubbles are identified as black disks. A particle-detection routine ("Particle analysis" method) is then performed on Fig. 11(c), which gives the area of each detected bubble. Black patches of area < 10 px^2 are not considered, as they cannot be clearly identified as bubbles. No circularity criterion is specified and incomplete drops on the edges are discarded. From the area of each bubble A_i, we extract their equivalent individual radius $R_i = \sqrt{A_i/\pi}$. We can therefore determine the bubble-radius distribution for each recorded image and monitor its evolution.

APPENDIX B: RAMAN SIGNAL PROCESSING

To detect the Raman shift k corresponding to the peak maximum shown in Fig. 4, we fit the Raman signal between $\nu = 960$ cm^{-1} and $\nu = 1060$ cm^{-1} with a standard Cauchy-Lorentz function: $f(\nu; I, k, \sigma) = I\sigma^2/((\nu - k)^2 + \sigma^2)$, where the intensity I, the peak center k, and its half width at midheight σ are fitting parameters. We then estimate the extent of the hydration reaction
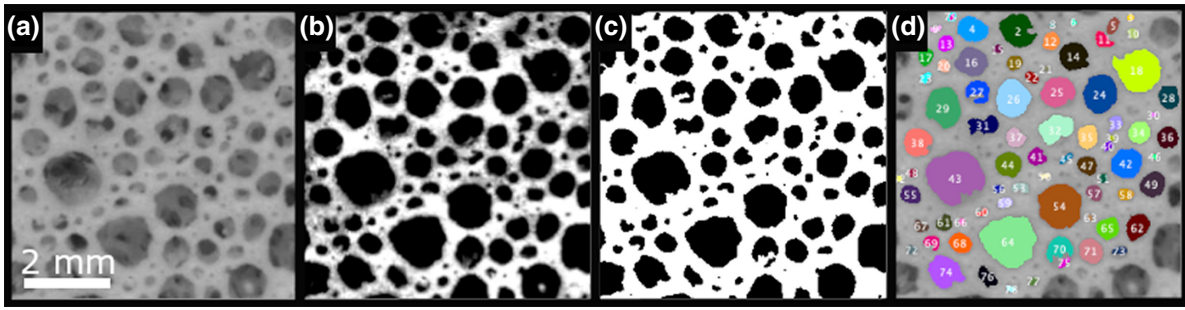
FIG. 11. The image-processing method: (a) the raw image; (b) the subtracted image (grayscale adjusted for clarity); (c) the binary image; and (d) the detected bubbles (numbered). Experimental conditions: $t = 1750$ s, $t_m = 60$ s, $\omega_m = 17$ Hz, TTAB 3 g/l, $c_{CA} = 0.5$ g/l.

as $\xi = 1 - [k(t) - k_f]/\Delta k_{\text{th}}$, where k_i and k_f denote the initial and final peak positions and $\Delta k_{\text{th}} = k_{\text{HH}} - k_{\text{DH}} = 6.3$ cm^{-1} is the difference between the hemihydrate and dihydrate peaks.

This procedure is slightly different from the multipeak analysis classically done in Raman spectroscopy. In our case, we can alternatively fit the signal with two Lorentzian functions at positions 1009.7 cm^{-1} (hemihydrate or plaster) and 1016.0 cm^{-1} (dihydrate or gypsum). The corresponding peak intensities I_{HH} (for hemihydrate) and I_{DH} (for dihydrate) are expected to be proportional to the concentration of these species [60]. To be quantitative, a precise calibration is, however, necessary, which requires a stable backscattered signal intensity, which is not the case here.

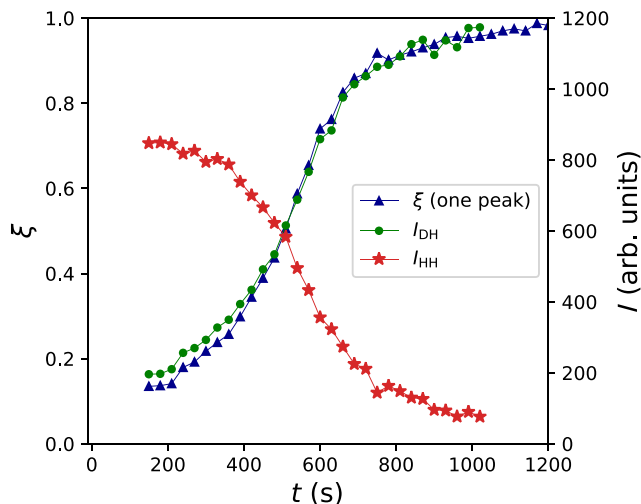Figure 12 shows an example of the evolution of the hemihydrate and dihydrate intensities I_{HH} and I_{DH}, together with the extent of the reaction ξ, obtained for a foamed sample without retardant. We observe that the three quantities vary accordingly, despite intensity fluctuations during the experiment.

In our study, we therefore focus on the single-peak analysis, as it is more straightforward and less demanding in terms of peak intensity, which is usually smaller in the foamed samples.

FIG. 12. The evolution of the hemihydrate I_{HH} and dihydrate I_{DH} intensities (right axis, from two-peak analysis), together with the extent of the reaction ξ (left axis, one-peak analysis). Experimental conditions: foamed and turned sample without retardant, $t_m = 60$ s, $\omega_m = 17$ Hz. The time interval between two measurements is 30 s.

[1] K. Ramamurthy, E. K. Kunhanandan Nambiar, and G. Indu Siva Ranjani, A classification of studies on properties of foam concrete, Cem. Concr. Compos. **31**, 388 (2009).

[2] A. Çolak, Density and strength characteristics of foamed gypsum, Cem. Concr. Compos. **22**, 193 (2000).

[3] J. Zhang, W. Liu, O. Gauthier, S. Sourice, P. Pilet, G. Rethore, K. Khairoun, J.-M. Bouler, F. Tancret, and P. Weiss, A simple and effective approach to prepare injectable macroporous calcium phosphate cement for bone repair: Syringe-foaming using a viscous hydrophilic polymeric solution, Acta Biomater. **31**, 326 (2016).

[4] Z. Zhang, J. L. Provis, A. Reid, and H. Wang, Geopolymer foam concrete: An emerging material for sustainable construction, Constr. Build. Mater. **56**, 113 (2014).

[5] C. Bai and P. Colombo, Processing, properties and applications of highly porous geopolymers: A review, Ceram. Int. **44**, 16103 (2018).

[6] H. K. Kim, J. H. Jeon, and H. K. Lee, Workability, and mechanical, acoustic and thermal properties of lightweight aggregate concrete with a high volume of entrained air, Constr. Build. Mater. **29**, 193 (2012).

[7] E. Ebaretonbofa and J. R. G. Evans, High porosity hydroxyapatite foam scaffolds for bone substitute, J. Porous Mater. **9**, 257 (2002).

[8] M. Scheffler and P. Colombo, *Cellular Ceramics* (Wiley, Weinheim, 2005).

[9] A. R. Studart, U. T. Gonzenbach, E. Tervoort, and L. J. Gauckler, Processing routes to macroporous ceramics: A review, J. Am. Ceram. Soc. **89**, 1771 (2006).

[10] B. Feneuil, N. Roussel, and O. Pitois, Optimal cement paste yield stress for the production of stable cement foams, Cem. Concr. Res. **120**, 142 (2019).

[11] V. Langlois, V. H. Trinh, C. Lusso, C. Perrot, X. Chateau, Y. Khidas, and O. Pitois, Permeability of solid foam: Effect of pore connections, Phys. Rev. E **97**, 053111 (2018).

[12] V. Langlois, A. Kaddami, O. Pitois, and C. Perrot, Acoustics of monodisperse open-cell foam: An experimental and numerical parametric study, J. Acoust. Soc. Am. **148**, 1767 (2020).

[13] I. Cantat, S. Cohen-Addad, F. Elias, F. Graner, R. Höhler, O. Pitois, F. Rouyer, and A. Saint-Jalmes, *Foams: Structure and Dynamics* (Oxford University Press, Oxford, 2013).

[14] B. Feneuil, P. Aimedieu, M. Scheel, J. Perrin, N. Roussel, and O. Pitois, Stability criterion for fresh cement foams, Cem. Concr. Res. **125**, 105865 (2019).

[15] E. Roch Isern and G. L. Messing, Direct foaming and seeding of highly porous, lightweight gypsum, J. Mater. Res. **31**, 2244 (2016).

[16] A. J. Lewry and J. Williamson, The setting of gypsum plaster. Part I: The hydration of calcium sulphate hemihydrate, J. Mater. Sci. **29**, 5279 (1994).

[17] C. Solberg and S. Hansen, Dissolution of $CaSO_4 \cdot 1/2H_2O$ and precipitation of $CaSO_4 \cdot 2H_2O$: A kinetic study by synchrotron x-ray powder diffraction, Cem. Concr. Res. **31**, 641 (2001).

[18] J. W. Bullard, H. M. Jennings, R. A. Livingston, A. Nonat, G. W. Scherer, J. S. Schweitzer, K. L. Scrivener, and J. J. Thomas, Mechanisms of cement hydration, Cem. Concr. Res. **41**, 1208 (2011).

[19] L. Amathieu and R. Boistelle, Crystallization kinetics of gypsum from dense suspension of hemihydrate in water, J. Cryst. Growth **88**, 183 (1988).

[20] A. J. Lewry and J. Williamson, The setting of gypsum plaster. Part II: The development of microstructure and strength, J. Mater. Sci. **29**, 5524 (1994).

[21] V. Fainerman and E. Lucassen-Reynders, Adsorption of single and mixed ionic surfactants at fluid interfaces, Adv. Colloid Interface Sci. **96**, 295 (2002).

[22] J. Peng, J. Qu, J. Zhang, M. Chen, and T. Wan, Adsorption characteristics of water-reducing agents on gypsum surface and its effect on the rheology of gypsum plaster, Cem. Concr. Res. **35**, 527 (2005).

[23] H. Li, H. Zhang, L. Li, Q. Ren, X. Yang, Z. Jiang, and Z. Zhang, Utilization of low-quality desulfurized ash from semi-dry flue gas desulfurization by mixing with hemihydrate gypsum, Fuel **255**, 115783 (2019).

[24] M. Mahmoud, M. Rashad, I. Ibrahim, and E. Abdel-Aal, Crystal modification of calcium sulfate dihydrate in the presence of some surface-active agents, J. Colloid Interface Sci. **270**, 99 (2004).

[25] J.-R. Hill and J. Plank, Retardation of setting of plaster of Paris by organic acids: Understanding the mechanism through molecular modeling, J. Comput. Chem. **25**, 1438 (2004).

[26] A. Ersen, A. Smith, and T. Chotard, Effect of malic and citric acid on the crystallisation of gypsum investigated by coupled acoustic emission and electrical conductivity techniques, J. Mater. Sci. **41**, 7210 (2006).

[27] R. Magallanes-Rivera, J. Escalante-García, and A. Gorokhovsky, Hydration reactions and microstructural characteristics of hemihydrate with citric and malic acid, Constr. Build. Mater. **23**, 1298 (2009).

[28] M. Lanzón and P. A. García-Ruiz, Effect of citric acid on setting inhibition and mechanical properties of gypsum building plasters, Constr. Build. Mater. **28**, 506 (2012).

[29] K. M. Song, J. Mitchell, H. Jaffel, and L. F. Gladden, Simultaneous monitoring of hydration kinetics, microstructural evolution, and surface interactions in hydrating gypsum plaster in the presence of additives, J. Mater. Sci. **45**, 5282 (2010).

[30] S. Chatterji and J. W. Jeffery, Volume expansion of setting plaster, Trans. Faraday Soc. **60**, 1947 (1964).

[31] N. Politova, S. Tcholakova, Z. Valkova, K. Golemanov, and N. D. Denkov, Self-regulation of foam volume and bubble size during foaming via shear mixing, Colloids Surf A: Physicochem. Eng. Asp. **539**, 18 (2018).

[32] W. Drenckhan and A. Saint-Jalmes, The science of foaming, Adv. Colloid Interface Sci. **222**, 228 (2015).

[33] See the Supplemental Material at http://link.aps.org/supplemental/10.1103/PhysRevApplied.18.034078 for a video of the experiment of Fig. 3.

[34] J. Schindelin, I. Arganda-Carreras, E. Frise, V. Kaynig, M. Longair, T. Pietzsch, S. Preibisch, C. Rueden, S. Saalfeld, B. Schmid, J.-Y. Tinevez, D. J. White, V. Hartenstein, K. Eliceiri, P. Tomancak, and A. Cardona, FIJI: An open-source platform for biological-image analysis, Nat. Methods **9**, 676 (2012).

[35] H. C. Cheng and R. Lemlich, Errors in the measurement of bubble size distribution in foam, Ind. Eng. Chem. Fundam. **22**, 105 (1983).

[36] Y. Wang and S. J. Neethling, The relationship between the surface and internal structure of dry foam, Colloids Surf. A: Physicochem. Eng. Asp. **339**, 73 (2009).

[37] M. Emília Rosa and M. A. Fortes, Coarsening of two-dimensional foams confined by walls, Philos. Mag. A **79**, 1871 (1999).

[38] A. S. Gittings and D. J. Durian, Statistics of bubble rearrangement dynamics in a coarsening foam, Phys. Rev. E **78**, 066313 (2008).

[39] M. U. Vera, A. Saint-Jalmes, and D. J. Durian, Scattering optics of foam, Appl. Opt. **40**, 4210 (2001).

[40] L. P. Sarma, P. S. R. Prasad, and N. Ravikumar, Raman spectroscopic study of phase transitions in natural gypsum, J. Raman Spectrosc. **29**, 851 (1998).

[41] N. Prieto-Taboada, O. Gómez-Laserna, I. Martínez-Arkarazo, M. A. Olazabal, and J. Madariaga, Raman spectra of the different phases in the $CaSO_4$-H_2O system, Anal. Chem. **86**, 10131 (2014).

[42] U. T. Gonzenbach, A. R. Studart, E. Tervoort, and L. J. Gauckler, Macroporous ceramics from particle-stabilized wet foams, J. Am. Ceram. Soc. **90**, 16 (2007).

[43] I. Lesov, S. Tcholakova, and N. Denkov, Factors controlling the formation and stability of foams used as precursors of porous materials, J. Colloid Interface Sci. **426**, 9 (2014).

[44] A. K. S. Chesterton, G. D. Moggridge, P. A. Sadd, and D. I. Wilson, Modelling of shear rate distribution in two planetary mixtures for studying development of cake batter structure, J. Food. Eng. **105**, 343 (2011).

[45] E. A. Pachon-Rodriguez and J. Colombani, Pure dissolution kinetics of anhydrite and gypsum in inhibiting aqueous salt solutions, AIChE J. **59**, 1622 (2013).

[46] M. J. Ridge, Hydration of calcium sulphate hemihydrate, Nature **204**, 70 (1964).

[47] G. Dumazer, V. Narayan, A. Smith, and A. Lemarchand, Modeling gypsum crystallization on a submicrometric scale, J. Phys. Chem. C **113**, 1189 (2009).

[48] M. D. Vlad, R. Torres, J. López, M. Barracó, J. A. Moreno, and E. Fernández, Does mixing affect the setting of injectable bone cement? An ultrasound study, J. Mater. Sci.: Mater. Med. **18**, 347 (2007).

[49] D. Han and R. D. Ferron, Influence of high mixing intensity on rheology, hydration, and microstructure of fresh state cement paste, Cem. Concr. Res. **84**, 95 (2016).

[50] R. C. Sonntag and W. B. Russel, Structure and breakup of flocs subjected to fluid stresses: I. Shear experiments, J. Colloid Interface Sci. **113**, 399 (1986).

[51] J. B. Hipp, J. J. Richards, and N. J. Wagner, Direct measurements of the microstructural origin of shear-thinning in carbon black suspensions, J. Rheol. **65**, 145 (2021).

[52] A. Saint-Jalmes, Physical chemistry in foam drainage and coarsening, Soft Matter **2**, 836 (2006).

[53] H. Bey, F. Wintzenrieth, O. Ronsin, R. Höhler, and S. Cohen-Addad, Stabilization of foams by the combined effects of an insoluble gas species and gelation, Soft Matter **13**, 6816 (2017).

[54] L. Zhang, C. Liu, L. Liu, and H. Zhang, Study on early hydration of gypsum-based materials containing different chemical admixtures by isothermal calorimetry and oscillation rheology, J. Therm. Anal. Calorim. **147**, 6099 (2022).

[55] A. Mikhailovskaya, V. Trappe, and A. Salonen, Colloidal gelation, a means to study elasto-capillarity effects in foam, Soft Matter **16**, 2249 (2020).

[56] F. Gorlier, Y. Khidas, A. Fall, and O. Pitois, Optimal strengthening of particle-loaded liquid foams, Phys. Rev. E **95**, 042604 (2017).

[57] D. Torréns-Martín, L. Fernández-Carrasco, and S. Martínez-Ramírez, Hydration of calcium aluminates and calcium sulfoaluminate studied by Raman spectroscopy, Cem. Concr. Res. **47**, 43 (2013).

[58] F. Liu, Z. Sun, and C. Qi, Raman spectroscopy study on the hydration behaviors of Portland cement pastes during setting, J. Mater. Civil Eng. **27**, 04014223 (2015).

[59] F. Krauss Juillerat, U. T. Gonzenbach, P. Elser, A. R. Studart, and L. J. Gauckler, Microstructural control of self-setting particle-stabilized ceramic foams: Microstructural control of particle-stabilized foams, J. Am. Ceram. Soc. **94**, 77 (2011).

[60] B. P. Kafle, in: *Chemical Analysis and Material Characterization by Spectrophotometry* (Elsevier, Amsterdam, 2020), Chap. 8, p. 245.